frontiers | Frontiers in Earth Science

TYPE Original Research
PUBLISHED 28 December 2023
DOI 10.3389/feart.2023.1287151

OPEN ACCESS

EDITED BY
Xuelong Li,
Shandong University of Science and Technology, China

REVIEWED BY
Jinbo Miao,
Hebei University of Engineering, China
Zhenbo Zhang,
Shijiazhuang Tiedao University, China
Zhitian Xie,
Beijing Municipal Engineering Research Institute, China
Xiaopu Cui,
Beijing University of Technology Beijing, China, in collaboration with reviewer ZX

*CORRESPONDENCE
Fengnian Wang,
wangfn_bj@163.com

RECEIVED 01 September 2023
ACCEPTED 19 October 2023
PUBLISHED 28 December 2023

CITATION
Qiang S, Zhao L, Wang X, Li X and Wang F (2023), Analysis of face stability for shallow shield tunnels in sand.
Front. Earth Sci. 11:1287151.
doi: 10.3389/feart.2023.1287151

Analysis of face stability for shallow shield tunnels in sand

Sihan Qiang[1], Lizhi Zhao[1], Xuehai Wang[1], Xiaoming Li[1] and Fengnian Wang[2,3]*

[1]5TH Engineering LTD. of the First Highway Engineering Bureau CCCC, Beijing, China, [2]Shanxi Transportation Technology Research and Development Co., Ltd., Taiyuan, China, [3]School of Earth Sciences and Engineering, Hohai University, Nanjing, China

The stability of the tunnel face is the key problem in shield tunnel construction. This paper focuses on the face stability of a shallow tunnel in sand. Numerical simulation and theoretical analysis are combined to study the limit support pressure and failure zone. Firstly, numerical simulation is employed to study the collapse of the tunnel face, obtaining the limit support pressure and collapse zone. A new failure model suitable for shallow tunnels is constructed based on these numerical simulations. Then, an analytic solution for the limit support pressure is derived using limit analysis upper bound theory. The accuracy and applicability of this proposed model are verified by comparing it with numerical results and classical analytical models. Through this research, it is found that the proposed model provides a more accurate description of situations where soil arches cannot be formed for shallow tunnels in sand, leading to higher accuracy in calculating the limit support pressure. The influence of various factors on stability of the tunnel face is analyzed, revealing mechanisms of tunnel face collapse.

KEYWORDS

shallow tunnel, sand stratum, tunnel face stability, limit analysis method, sand

1 Introduction

Recently, tunnels have been constructed mainly using the shield method. During shield construction, tunnel face is usually stabilized by controlling the pressure in soil or slurry chamber. The stability of the tunnel face is typically ensured by controlling the pressure in the soil chamber or slurry chamber during shield tunneling (Chen et al., 2018; Wang et al., 2021a). Insufficient support pressure can easily lead to collapse of the excavation face, resulting in significant economic losses. Therefore, determining the values of soil chamber pressure and slurry chamber pressure is crucial for the control of shield tunneling (Liao et al., 2009). Currently, many researchers have employed a combination of model test, numerical simulations, and theoretical analysis to study the limit support pressure (σ_T) of collapse, the minimum support pressure to maintain stability of excavation face.

Researchers have conducted various physical experiments to study σ_T and the failure zone shapes (Kirsch, 2010; Messerli et al., 2010; Chen et al., 2013; Wang et al., 2021b). Some researchers have also conducted centrifuge model tests to study collapse mechanism of tunnel face, yielding significant research outcomes (Atkinson et al., 1977; Chambon and Corte, 1994; Meguid et al., 2008; Idinger et al., 2011; Li et al., 2023). Physical model tests not only provide validation for numerical simulation results but also establish a solid foundation for theoretical models. Numerical simulation, due to their advantages of low cost, high efficiency, and repeatability, are often used as a complement to model experiments and are widely applied in tunnel engineering. Currently, the main numerical models used are the continuum models (Senent et al., 2013; Li et al., 2019; Li et al., 2020; Liu H. et al., 2023) and the discrete element models. The

TABLE 1 Calculation parameters.

Cases	Tunnel diameter D (m)	Cover ratio C/D	Unit weight γ (kN/m^3)	Elastic modulus E (MPa)	Poisson ratio v	Friction angle φ(°)	Cohesion c(kPa)
1~4	6	0.5	18	20	0.35	25,30,35,40	0
5~8		0.75				25,30,35,40	
9~12		1.0				25,30,35,40	
12~16		1.25				25,30,35,40	

discrete element method has also been extensively employed to investigate tunnel face instability (Funatsu et al., 2008; Chen et al., 2011; Zhang et al., 2011; Liu and Li, 2023), since its capability to handle mechanics problems involving discontinuous materials. Scholars have made significant achievements in various aspects, including the calculation of σ_T and definition of collapse zone.

Theoretical analysis is an essential approach to obtain the σ_T of excavation face, and scholars have been devoted themselves to proposing theoretical solutions for calculating the σ_T. Currently, there are two main methods. The limit equilibrium method assumes a failure mode and solves the σ_T based on the equilibrium conditions of forces. Scholars have proposed different failure models and obtained σ_T for different soil layers (Horn, 1961; Murayama et al., 1966; Anagnostou and Kovári, 1994; Arthur et al., 1994; Yu et al., 2020; Zhang et al., 2020; Liu S. et al., 2023; Zhang et al., 2023). The limit analysis method mainly acquire the limit support pressure from an energy perspective. (Leca and Dormieux, 1990) proposed failure mechanisms consisting of a single truncated cone or double truncated cones and derived the theoretical solutions of σ_T based on the limit analysis upper bound theory. Based on the model proposed by (Leca and Dormieux, 1990; Soubra et al., 2008) proposed a 3D failure model with multiple truncated cones and found that increasing the number of truncated cones beyond five had little effect on computational accuracy. This failure model has been widely cited by scholars. (Mollon et al., 2011b) using a logarithmic spiral model and spatial discretization technique, established a new 2*D* failure model that further improved the calculation accuracy. In addition, (Mollon et al., 2011a) proposed a 3*D* horn-shaped collapse model based on a multi-block model and spatial discretization technique, which overcame non-overlap of the multi-truncated cones model at excavation face and further improves the accuracy of the model.

Based on model tests and numerical simulations, researchers have abstracted failure models of excavation face instability during shield tunneling and derived analytical solutions for the σ_T. However, there are still some unresolved issues that deserve attention. For shallow tunnels, the σ_T obtained by the limit equilibrium theory tends to be higher than the experimental values, which can easily lead to passive instability of tunnel face. On the other hand, models based on limit analysis theory can form soil arching even in case of shallow tunnels. However, in experiments, the failure zone may still extend to the ground surface for loose sand with cover ratio greater than 2.0, resulting in underestimated soil pressures (Di et al., 2022a).

In this paper, based on the numerical models, a new collapse model for shallow tunnel in sand is proposed. The analytical solutions are derived using the limit analysis method. The proposed theoretical model is compared with numerical models and existing models to validate its applicability and accuracy. Finally, using the proposed model, the influence of various factors on stability of tunnel face is analyzed, and the mechanism of collapse of tunnel face is revealed.

2 Numerical simulation

2.1 Numerical models

The finite difference software FLCA3D is used to study limit support pressure σ_T and failure zone for shallow tunnel in this section. A total of 16 cases were considered in Table 1 to investigate the effect of cover ratio C/D and friction angle φ on tunnel face stability. The soil

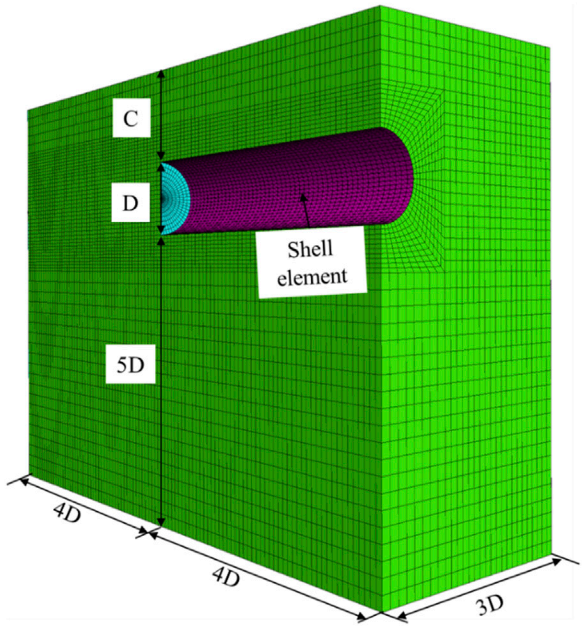

FIGURE 1
Numerical model.

parameters are as described below: Unit weight $\gamma = 18$ kN/m^3, Young's modulus $E = 20$ MPa, Poisson's ratio $v = 0.35$, and cohesion $c = 0$ kPa.

As shown in Figure 1, a semi-model approach was adopted, taking into account computational efficiency. The dimensions of the model are the following: width 3*D*, length 8*D*, height 6*D* + *C*, where *D* is tunnel diameter and *C* is the tunnel burial depth. The boundary conditions of the model are as follows: fixed at the bottom, constrained normal displacement at the sides, and free at the top. The soil material was modeled using solid elements, assuming it follows the Mohr-Coulomb criterion. To simulate the lining, shell elements with $E = 20$ GPa, $v = 0.17$ and a thickening of 0.35 m were used.

To simulate, proceed as follows:

(1) Create soils layers and initialize the soil stress.
(2) To simplify the simulation process, a one-step excavation method is used, with lining applied simultaneously.
(3) Apply a support pressure (P_T) to the tunnel face, where the value of the P_T is equal to the horizontal stress in the center of the tunnel face.
(4) Reduce the P_T and plot the curve of P_T versus horizontal displacement (Δ_h) of the center of the excavation face.
(5) When the P_T sharply increases, the corresponding support pressure is considered as the limit support pressure (σ_T) (Li et al., 2022).

2.2 Numerical results

2.2.1 Limit support pressure

In the simulation, when the support pressure sharply increases, the corresponding support pressure is considered as the limit support pressure. The double tangent method proposed by Li et al. (2019) is used to determine the limit support pressure. The specific method is as follows: make the curve of support pressure and excavation face displacement, make the tangent line of the descending section and the horizontal section respectively, and the intersection point of the two is the limit support pressure. Figures 2A–D shows the relationship between Δ_h and P_T for varying cover ratios *C/D*. Under varying cover ratios, the support pressure gradually decreases with increasing φ. From the results shown in Figure 2A, it can be observed that at $C/D = 0.5$ and $\varphi = 25^\circ$, the $\sigma_T = 17.85$ kPa. When the $\varphi = 30^\circ$, 35°, and 40°, the $\sigma_T =$ 12.75 kPa, 9.35 kPa, and 7 kPa, respectively. Figure 2B demonstrates that for $C/D = 0.75$, and $\varphi = 25^\circ$, 30°, 35°, and 40°, the $\sigma_T = 18.85$ kPa, 13.50 kPa, 9.85 kPa, and 7.00 kPa, respectively. Similarly, from Figures 2C, D, the σ_T can be obtained for cover ratios of 1.0 and 1.25, respectively.

Figure 3 illustrates the relationship between the σ_T and the φ (in radians) for different *C/D*. By comparing, it can be observed that there is an exponential relationship between the σ_T and the φ. The exponential function $\sigma_T = e^{a+b\varphi+c\varphi2}$ was used to fit the data, resulting in the following relationships: for $C/D = 0.5$, $\sigma_T = e^{4.91\text{-}5.32\varphi+1.54\varphi2}$, R^2=0.995; for $C/D =$ 0.75, $\sigma_T = e^{4.50\text{-}3.47\varphi-0.25\varphi2}$, $R^2 = 0.992$; for $C/D = 1.0$, σ_T=$e^{4.11\text{-}1.74\varphi-1.94\varphi2}$, $R^2 =$ 0.987; for $C/D = 1.25$, σ_T=$e^{3.88\text{-}0.561\varphi+3.15\varphi2}$, R^2=0.981.

The fitting results show that the coefficients *a, b,* and *c* have a strong linear relationship with the cover ratio *C/D*, as illustrated in Figure 4. The correlation between the coefficient *a* and the *C/D* can be expressed as $a = 5.57–1.39C/D$, R^2=0.978. The correlation between the coefficient *b* and the *C/D* is as follows: $b = -8.38 +$ $6.42C/D$, R^2=0.983. The correlation between coefficient *c* and *C/D* is as follows: $c = 4.51–6.09C/D$, R^2= 0.989. Therefore, the correlation between the σ_T and *C/D* and φ is as follows:

$$\sigma_T(\mathrm{C/D}, \varphi) = e^{(5.57-1.39\mathrm{C/D})+(-8.38+6.42\mathrm{C/D})\varphi+(4.51-6.09\mathrm{C/D})\varphi2} \quad (1)$$

The validity range of Formula (1) is $C/D \le 1.25$ and friction angle $25^\circ \le \varphi \le 40^\circ$.

Figure 5 shows the variation of σ_T with respect to the *C/D*. The solid line represents the results calculated based on Formula (1), while the dashed line presents the values obtained from numerical simulations. From the graph, it is obvious that in the range of C/D≤1.25, the σ_T obtained from the numerical simulations shows an approximately linear increase with the increase of the *C/D*. Similarly, the σ_T calculated based on the fitted equation also shows an approximately linear increase with the cover ratio. A comparison between the two reveals that the calculated results from the Formula (1) are larger than the numerical results, and the discrepancy between them increases as the *C/D* increases. For instance, when φ=25° and $C/D = 0.5$, the fitted result is approximately 1.62% higher than the numerical simulation result. When $\varphi = 30^\circ$ and $C/D = 1.25$, the fitted result is approximately 4.98% higher, and at φ=30° and *C/D*=1.25, the difference reaches a maximum of approximately 9.2%. It is worth noting that the results from Formula (1) are relatively conservative compared to the numerical calculation results, and the difference is within an acceptable range, indicating a relatively safe approach for engineering applications.

2.2.2 Failure zone

Figure 6 illustrates the shapes of the failure zone under different cover ratios *C/D* for an internal friction angle of 35°. The boundary of the failure zone is defined by the abrupt change in the displacement gradient (Zhang et al., 2015). It is obvious that when the *C/D*≤1.0, the collapse zone extends to ground surface. The failure zone can be divided into two parts: the lower failure zone and the upper failure zone. The

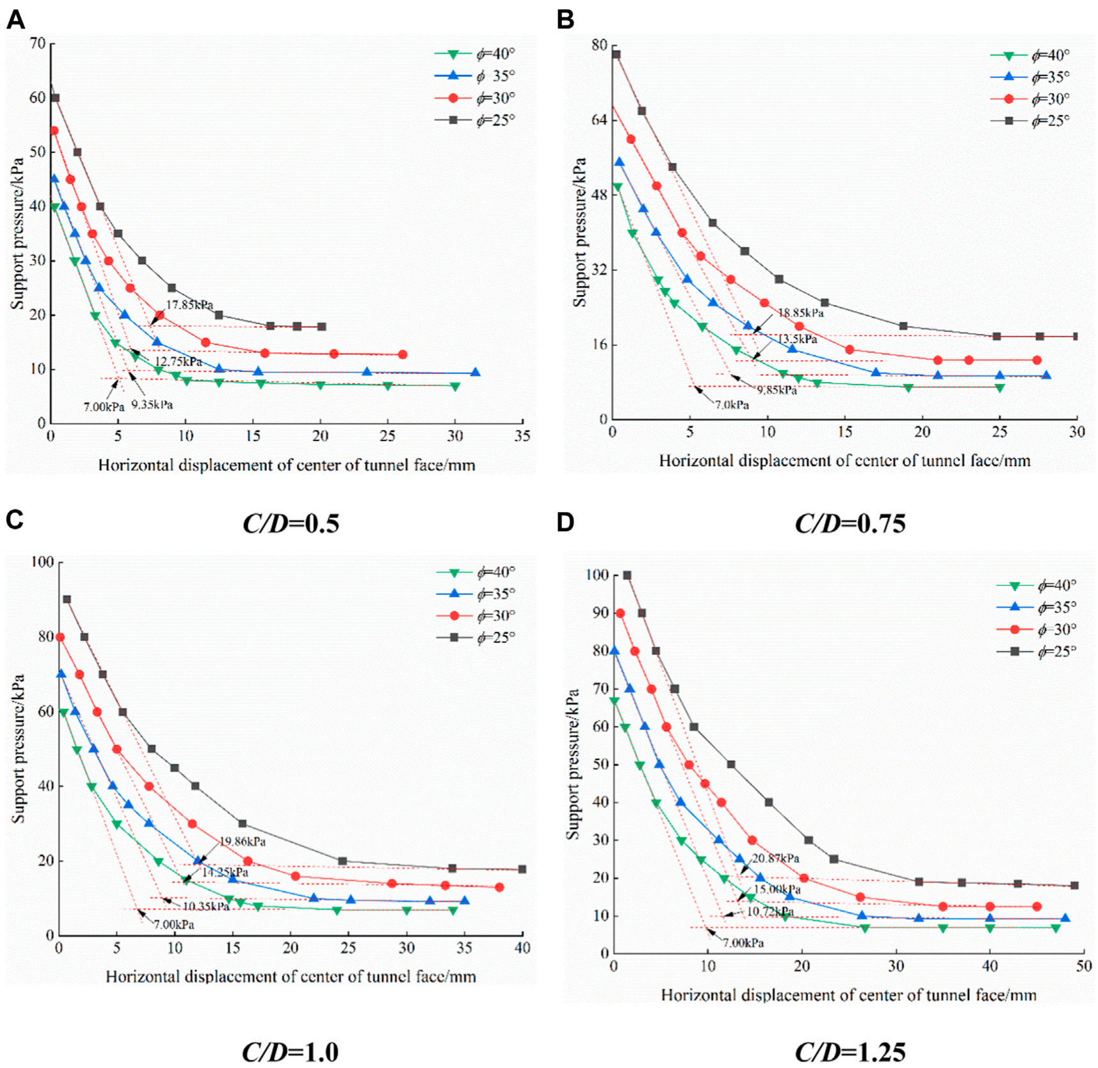

FIGURE 2
Relation curve of support pressure and horizontal displacement under different *C/D*. **(A)** C/D=0.5. **(B)** C/D=0.75. **(C)** C/D=1.0. **(D)** C/D=1.25.

lower failure zone exhibits a logarithmic curve shape, while the upper failure zone can be considered as an inverted round table shape (although the numerical simulation results are not apparent due to the stronger lining parameters near the tunnel face). The inverted round table can be further divided into a cylindrical-shaped failure core and a disturbed zone, which is consistent with the findings of (Li et al., 2018). When *C/D*>1.0, The collapse zone no longer extends to the surface; its shape consists mainly of the logarithmic curve-shaped lower failure zone and the upper soil arch zone.

3 Analytical model

3.1 Failure mechanism

Based on the numerical simulations, model tests (Di et al., 2022b), and engineering experience, a new *3D* collapse model for shallow shield tunnels has been proposed. As shown in Figure 7, tunnel diameter is *D*, cover depth is *C*, and support pressure is applied uniformly on the tunnel face. The failure zone is divided into upper and lower parts. The lower part adopts the classical five-cone model (Soubra et al., 2008): it assumes that the lower part consists of five rigid truncated cones, with each cone having a vertex angle of 2φ. The cones move along the axis of the cone and are constrained by the associated flow rules. The first truncated cone is formed by a rigid cone whose axis is at an Angle of α to the tunnel axis and a plane I which is at an angle of β_1 to the tunnel face. To ensure that the second cone completely coincides with the first cone at section I, the second cone is generated as a mirror image of the first cone and is cut by plane II, and so on for the third to fifth cones. The upper part of the collapse zone has a shape similar to an inverted round table. The core of the failure zone is in the shape of a cylinder, and the portion excluding the failure core is the disturbed zone. The boundary of the disturbed zone forms an angle θ with the horizontal direction. There is friction between the disturbed zone and the failure core, which reduces the vertical soil pressure.

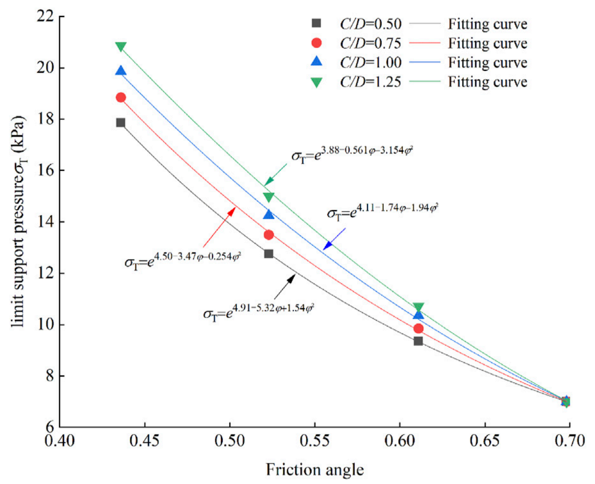

FIGURE 3
Relationship between limit support pressure and friction angle under different *C/D*.

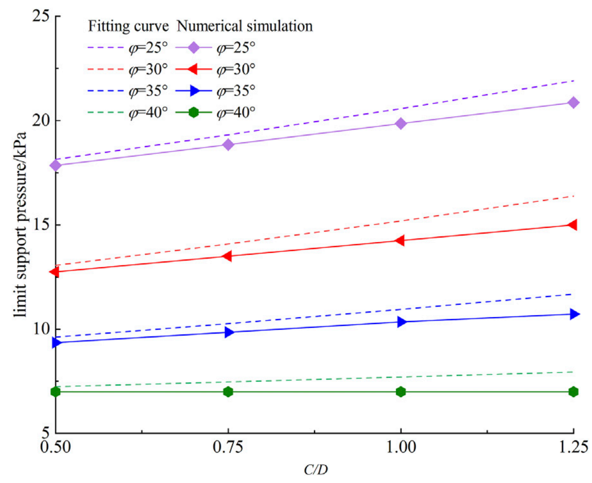

FIGURE 5
Relationship between limit support pressure and *C/D*.

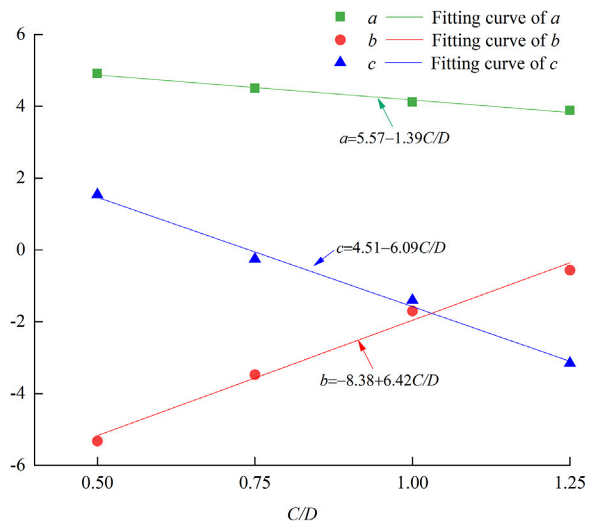

FIGURE 4
Relationship between coefficient (*a*,*b*,*c*) and *C/D*.

3.2 The vertical earth pressure σ_v

The effect of the upper collapse zone can be equivalently represented as a vertical earth pressure σ_v (Han et al., 2016). Based on geometric relationships, it is found that the intersection plane between the fifth truncated cone and the upper failure zone has an elliptical shape, with major axis a_6 and minor axis b_6. To simplify the calculation, we can approximate it as a circular shape with radius r, as proposed by (Li et al., 2020). The equivalent formula is given below:

$$r = \sqrt{a_6 b_6} \tag{2}$$

As shown in Figure 8, the upper failure zone is considered as an inverted round table, where the failure core is a cylindrical shape with a radius of r, and the remaining part is the disturbed zone. During the occurrence of failure, the disturbed zone forms an angle θ with the horizontal plane, exhibiting a tendency to slide downward, resulting in friction along the slip surface. The core of collapse zone tends to move downward and is constrained by the disturbed zone. Here, P_s represents the surface overload, and σ'_v represents the reactive force of σ_v.

To determine the magnitude of vertical soil pressure, we select any vertical plane passing through the axis of the truncated cone as the calculation diagram, such as Figure 9. The following assumptions are made: The soil follows the Mohr-Coulomb strength criterion. Coefficient of friction of the sliding surface *AD* and *BE* is $\tan\varphi$. Due to soil disturbed, the friction angle between the failure core and the disturbed zone is given by η ($\eta \le \varphi$). The ground overload P_s and the vertical soil pressure σ_s are both uniformly distributed loads.

The *ADF* section is taken as the object of force analysis, and the vertical equilibrium equation and the horizontal equilibrium equation are formulated to obtain the following equations:

$$\begin{cases} N\sin(\theta-\varphi) - T'\cos\eta - cC\cot\theta = 0 \\ W_2 + P_s C\cot\theta + T\sin\eta - N\cos(\varphi-\theta) = 0 \end{cases} \tag{3}$$

Where:

$$W_2 = \frac{\gamma C^2}{2}\cot\theta \tag{4}$$

The vertical equilibrium equation is formulated for the *ABFG* section as the object of study, yielding the following equation.

$$W_1 + P_s r - 2cC - 2T\sin\eta - \sigma_v r = 0 \tag{5}$$

Where:

$$W_1 = \frac{\gamma r C}{2} \tag{6}$$

When active failure occurs, the angle θ is given by $\theta = \pi/4 + \varphi/2$ by the Mohr-Coulomb criterion. The friction angle η can be obtained from Table 2 (Li et al., 2018). For sandy soil classified as VI rock mass, its range of values is between 0.3φ and 0.5φ.

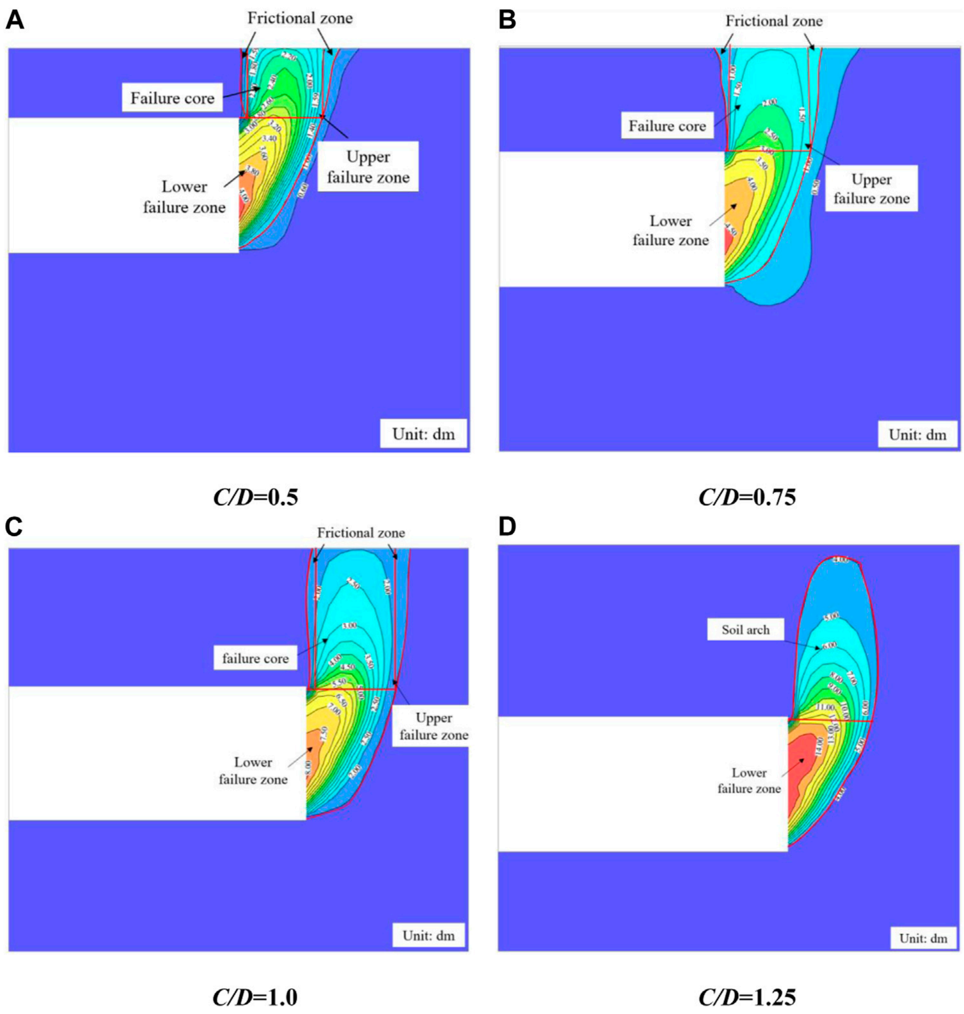

FIGURE 6
Failure zone under different *C/D* (φ = 35°unit:dm). **(A)** C/D=0.5. **(B)** C/D = 0.75. **(C)** C/D = 1.0. **(D)** C/D = 1.25.

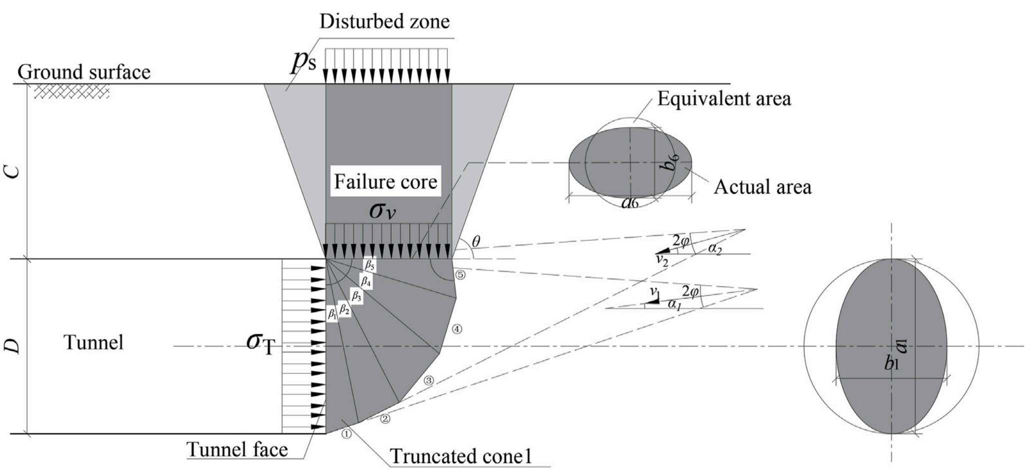

FIGURE 7
Proposed failure mechanism.

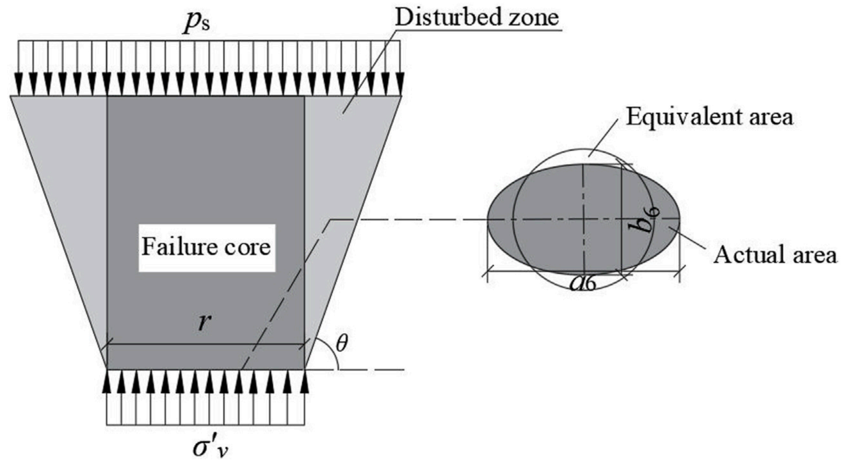

FIGURE 8
Upper failure mechanism.

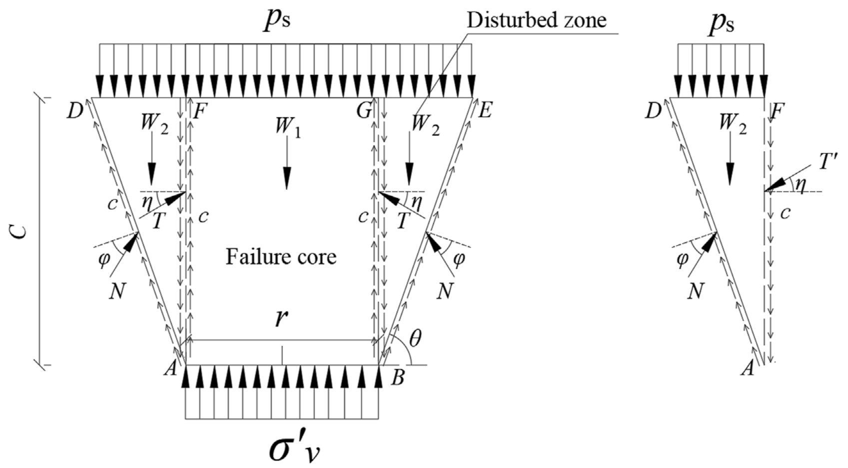

FIGURE 9
Calculation diagram of upper failure zone.

TABLE 2 η **value of all grades of surrounding rock.**

Grades of surrounding rock	I~III	IV	V	VI
η	0.9φ	$(0.7\sim0.9)\varphi$	$(0.5\sim0.7)\varphi$	$(0.3\sim0.5)\varphi$

By simultaneously solving Eqs 3–6, the vertical soil pressure σ_v can be obtained.

3.3 Limit support pressure

3.3.1 Limit analysis method

The limit analysis method derives the limit load from an energy perspective. An upper bound estimate of such loads is found by considering a kinematically admissible failure mechanism for which the power of the loads applied to the system is larger than the power that can be dissipated inside the system during its movement (Chen, 1975). Thus, When the tunnel face is stable, the following equation should satisfy:

$$P_e \leq P_v \tag{7}$$

Where P_e is the power of external forces and P_v is the dissipated power in the failure zone.

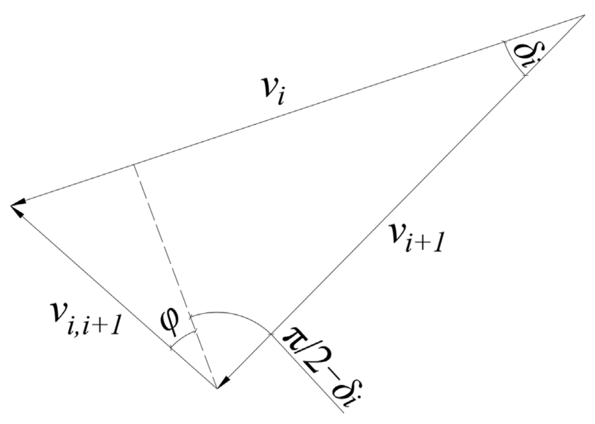

FIGURE 10
Velocity field of the proposed mechanism.

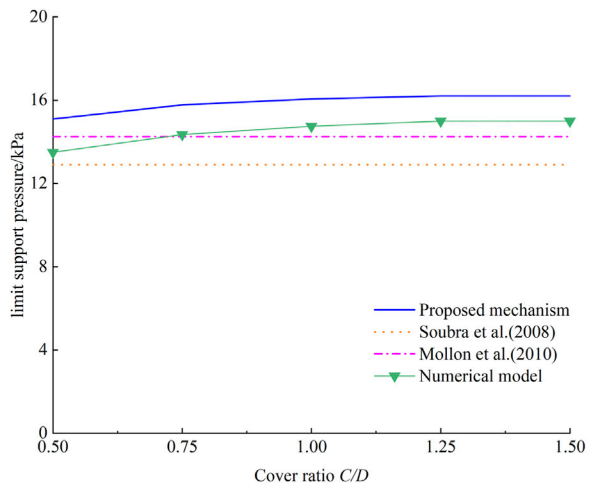

FIGURE 11
Comparison of proposed model with other models under different C/D.

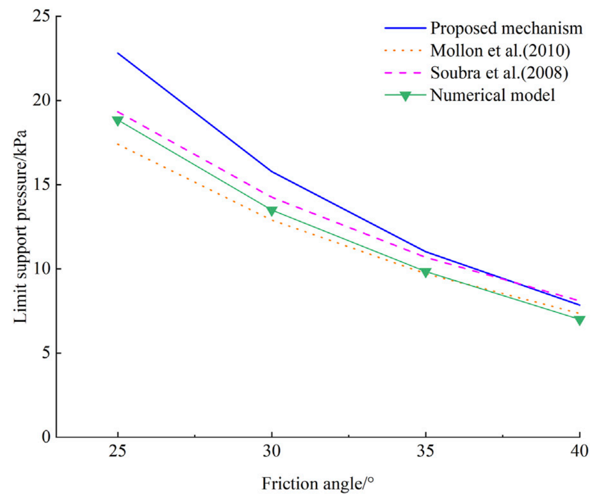

FIGURE 12
Comparison of proposed model with other models under different φ.

3.3.2 Geometric relationship

To calculate the internal and external powers in the failure zone, it is necessary to derive the geometric relationships. Based on these relationships, the angle α_i between the axis of the *i-the* truncated cone and the tunnel axis is given by Formula (8):

$$\alpha_i = \sum_{j=1}^{i-1} \beta_i + \delta_i \,(i = 2, 3, 4, 5) \tag{8}$$

The angles δ_i are as follows:

$$\delta_i = \begin{cases} \alpha, i = 1 \\ \beta_i - \delta_{i-1}, i = 2, 3, 4, 5 \end{cases} \tag{9}$$

Through analysis, it can be determined that the section obtained by the oblique intersection of each cone with the plane is an ellipse. The long axis, short axis, and area of the ellipse obtained by the *i-th* cone are denoted by a_i, b_i, and A_i, respectively, as given by Eqs 10–12.

$$a_i = \begin{cases} \dfrac{D}{2}, i = 1 \\ \dfrac{D}{2}\prod_{k=1}^{i}\dfrac{\cos(\delta_k + \varphi)}{\cos(\delta_{k+1} - \varphi)}, i = 2, 3, 4, 5 \\ a_5\dfrac{\cos(\beta_4 - \beta_3 + \beta_2 - \beta_1 + \alpha_1 + \varphi)}{\sin(2\beta_4 + 2\beta_2 + \alpha_1 + \varphi)}, i = 6 \end{cases} \tag{10}$$

$$b_i = \begin{cases} a_i\dfrac{\sqrt{\cos(\delta_i + \varphi)\cos(\delta_i - \varphi)}}{\cos\varphi}, i = 1, 2, 3, 4, 5 \\ a_6\dfrac{\sqrt{\sin\left(\sum_{j=1}^{5}\delta_i + \varphi\right)\sin\left(\sum_{j=1}^{5}\delta_i - \varphi\right)}}{\cos\varphi}, i = 6 \end{cases} \tag{11}$$

$$A_i = \pi a_i b_i \tag{12}$$

The volumes of *i-th* cones, denoted as V_i, can be expressed by formula (13):

$$V_i = \begin{cases} \dfrac{A_i h_i - A_{i+1} h_{i+1}}{3}, i = 1, 2, 3, 4 \\ \dfrac{A_5 h_5 - A_5 h_5'}{3}, i = 5 \end{cases} \tag{13}$$

Where:

$$\begin{cases} h_1 = \dfrac{D\cos(\alpha_1 + \varphi)\cos(\alpha_1 - \varphi)}{\sin 2\varphi} \\ h_2 = \dfrac{D\cos(\alpha_1 + \varphi)\cos(\beta_1 - \alpha_1 + \varphi)}{\sin 2\varphi} \\ h_i = h_2\prod_{j=2}^{i-1}\dfrac{\cos(\delta_{j+1} + \varphi)}{\cos(\delta_j - \varphi)}, i = 3, 4, 5 \\ h_5' = h_5\dfrac{\sin(2\beta_4 + 2\beta_2 + \alpha_1 - \varphi)}{\cos(\delta_5 - \varphi)} \end{cases} \tag{14}$$

10.3389/feart.2023.1287151

TABLE 3 Comparison between model test results and analytical solutions of limit support pressure.

c (kPa)	φ (°)	γ (kN/m^3)	D (m)	C/D	Test result	Proposed mechanism			
					kPa	c = 0kPa, φ = 38°	c = 5kPa, φ = 38°	c = 0kPa, φ = 42°	c = 5kPa, φ = 42°
0–5	38–42	16.1	5	0.5	3.6	6.65	0.1	5.13	stable
				0.5	3.5				
				1	3.5	6.71	0.02	5.14	stable
				1	3.0				
				1	3.3				
0–5	38–42	15.3	5	0.5	4.2	6.32	0.3	4.87	stable
				1	5.5	6.37	0.3	4.88	stable
0–5	38–42	16.0	10	1	7.4	13.44	6.76	10.32	4.62

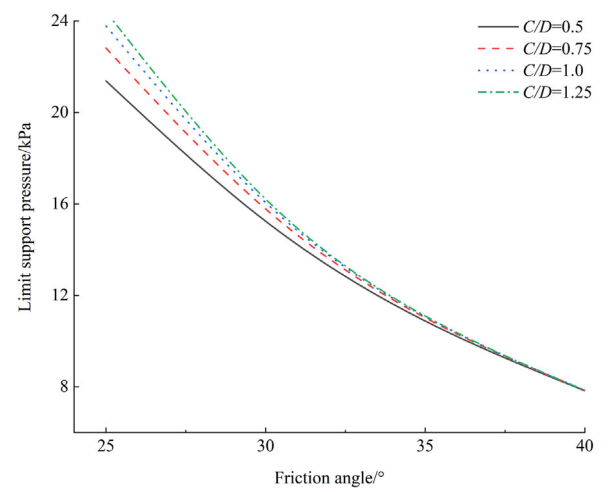

FIGURE 13
Influence of friction angle on limit support pressure under different *C/D*.

It is assumed that the velocity of each cone is parallel to its axis. The velocity of the *i-th* cone is denoted as v_i, and the relative velocity between the *i-th* cone and the *(i+1)-th* cone is denoted as $v_{i,i+1}$. The relationship between v_i, v_{i+1}, and $v_{i,i+1}$ is illustrated in Figure 10. the v_i, v_{i+1}, and $v_{i,i+1}$ can be expressed by formula (15) and (16).

$$v_i = v_1 \prod_{j=2}^{i} \frac{\cos\left(\delta_j + \varphi\right)}{\cos\left(\delta_{j+1} - \varphi\right)}, i \geq 2 \tag{15}$$

$$v_{i,i+1} = v_i \frac{\sin\left(2\delta_{j+1}\right)}{\cos\left(\delta_{j+1} - \varphi\right)}, i \geq 1 \tag{16}$$

3.3.3 Optimization of limit support pressure

The P_e is mainly composed of three parts: the power of support pressure P_T, the power of gravity in the failure zone P_γ, and the power of vertical load $P_{\sigma v}$, which can be expressed as follows:

$$P_e = P_T + P_\gamma + P_{\sigma_v} \tag{17}$$

P_T can be calculated using Eq. 18:

$$P_T = -A_1 \cos\alpha_1 \sigma_T v_1 \tag{18}$$

The power of gravity P_γ can be expressed using the following equation:

$$P_\gamma = \left[V_1 \sin\alpha_1 v_1 + V_2 \sin\left(2\beta_1 - \alpha_1\right) v_2 + V_3 \sin\left(2\beta_2 + \alpha_1\right) v_3 + V_4 \sin\left(2\beta_1 + 2\beta_3 - \alpha_1\right) v_4 + V_5 \sin\left(2\beta_2 + 2\beta_4 + \alpha_1\right) v_5\right]\gamma \tag{19}$$

The power of equivalent vertical pressure $P_{\sigma v}$ can be expressed using the following equation:

$$P_{\sigma_v} = A_6 \sin\left(2\beta_2 + 2\beta_4 + \alpha_1\right)\sigma_v v_5 \tag{20}$$

The dissipated power occurs mainly at the boundary of the collapse zone and between the truncated cones, which can be expressed by Formula (21):

$$P_v = \left[\frac{A_1 \cos\alpha_1}{\sin\varphi} v_1 - \frac{A_5 \sin\left(2\beta_2 + 2\beta_4 + \alpha_1\right)}{\sin\varphi} v_5\right] c \cos\varphi \tag{21}$$

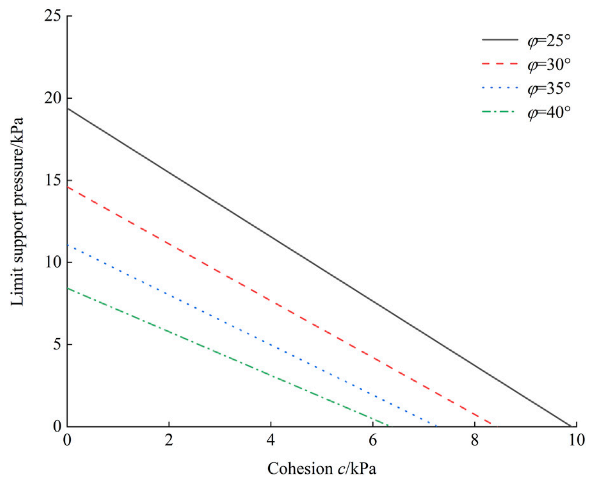

FIGURE 14
Influence of cohesion on limit support pressure under different φ.

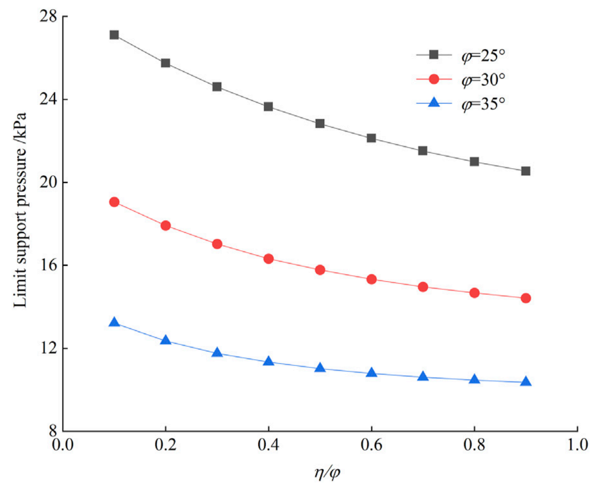

FIGURE 16
Influence of η/φ on limit support pressure under different φ.

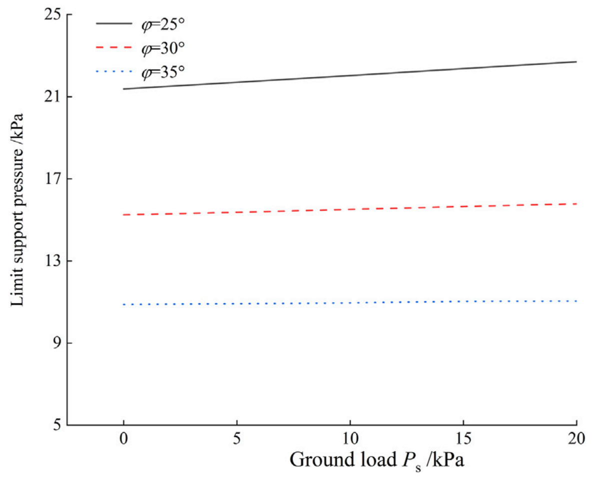

FIGURE 15
Influence of Ground load on limit support pressure under different.

By substituting Eqs 17–21 into Eq. 7, the following expression can be derived:

$$\sigma_T \geq \sigma_v N_{\sigma_v} + \gamma D N_\gamma + c N_c \tag{22}$$

Where:

$$\begin{cases} N_{\sigma_v} = \dfrac{A_6 \sin(2\beta_2 + 2\beta_4 + \alpha_1)}{A_1 \cos\alpha_1} \dfrac{v_5}{v_1} \\ N_\gamma = \left[V_1 \sin\alpha_1 v_1 + V_2 \sin(2\beta_1 - \alpha_1) v_2 + V_3 \sin(2\beta_2 + \alpha_1) v_3 \right. \\ \left. + V_4 \sin(2\beta_1 + 2\beta_3 - \alpha_1) v_4 + V_5 \sin(2\beta_2 + 2\beta_4 + \alpha_1) v_5\right] / (DA_1 \cos\alpha_1 v_1) \\ N_c = \dfrac{N_{\sigma_v} - 1}{\tan\varphi} \end{cases} \tag{23}$$

Formula (23) reveals that the σ_T depends on the geometric characteristics of the failure model (α_1, β_1 to β_5, C, D) and the soil parameters (c, φ). Therefore, the upper-bound method of the σ_T can be obtained through optimization theory. By considering the geometric characteristics of the failure model (α_1, β_1 to β_5) as optimization variables and maximizing the σ_T as the optimization objective, the value of σ_T can be determined:

$$\sigma_T = \max_{\alpha_1,\beta_1,\beta_2,\beta_3,\beta_4,\beta_5} \sigma_v N_{\sigma_v} + \gamma D N_\gamma + c N_c \tag{24}$$

4 Comparison

To verify the accuracy of the proposed model in the paper, it is compared with numerical models, classical analytical models, and model tests.

4.1 Comparing with numerical model and existing models

In Figure 11, a comparison is made between the proposed theoretical model, existing theoretical and numerical models, and model tests under the condition of an internal friction angle of 30° and η/φ = 0.5. From the graph, it can be observed that both the proposed model and the numerical model show an increase in the σ_T with an increase in the cover ratio, and the trends are similar. When the cover ratio reaches 1.25, the increase in the σ_T becomes less significant. (Soubra et al., 2008; Mollon et al., 2011a) also found that the σ_T does not change significantly beyond a cover ratio of 0.5. A comparison reveals that when the cover ratio is 0.5, the σ_T obtained from the proposed model is approximately 18% higher than the numerical results. As the cover ratio increases, the difference between the two approaches becomes smaller. When the cover ratio is 1.5, the proposed model yields approximately 8% higher results compared to the numerical simulation. The main reason for these discrepancies is that, based on model tests and engineering practice, the soil arch cannot form an arch for shallow tunnels, resulting in soil collapse to the ground and an increased vertical soil pressure. However, this phenomenon cannot be accurately simulated using a continuous medium model, leading to an underestimation of the vertical soil pressure. As the embedment ratio increases, the difference between the two models diminishes gradually due to the gradual emergence of the arching effect. Comparison with (Soubra et al., 2008; Mollon et al., 2011a), the proposed model yields approximately 13.7% and 25% higher results, respectively. The main reason for these differences is that (Soubra et al., 2008; Mollon et al., 2011a) prematurely assume the formation of an arching effect in soil with smaller friction angles, which contradicts experimental results and engineering practices.

In Figure 12, the results of different theoretical calculations for the variation of σ_T with φ are given for cover ratio $C/D = 0.75$ and $\eta/\varphi = 0.5$. It can be observed that all the results exhibit a nonlinear decrease with the increase of the φ. In terms of numerical values, when the $\varphi = 25^{\circ}$, the differences in σ_T obtained by the four models are the largest, while the differences are the smallest when the $\varphi = 40^{\circ}$. In addition, compared to the other models the proposed model gives higher σ_T. The main reason for these phenomena is that when the φ is small, the soil arch can't be formed, resulting in a higher vertical soil pressure. As the φ increases, the formation of the soil arch becomes easier, and the limit support pressure calculated by different models tend to converge.

4.2 Comparing with model experiments

Centrifuge tests results conducted by (Chambon and Corte, 1994) using sand are shown in Table 3. The sand parameters are as follows: $\varphi = 38^{\circ}$–42°, $c = 0$~5 kPa. As shown in the table, when the $\varphi = 38^{\circ}$ and the $c = 0$ kPa, the σ_T proposed in the paper is significantly higher than that obtained experimentally. With an increase in cohesion, the reduction in ultimate support force becomes more pronounced. When the cohesive strength reaches 5 kPa, the excavation face can stabilize itself. It should be noted that the soil parameters provided by (Chambon and Corte, 1994) are given as ranges, making it difficult to make accurate comparisons. However, the calculated results in this study include the experimental values, which demonstrates the validity of the proposed model.

5 Analysis

By comparison, it is found that the proposed model in this study is agrees well with numerical models and classical models. Especially in terms of shallow tunnel in sand, this model can more accurately describe the failure mode and provide more precise solutions. This section focuses on analyzing the influence of various factors on the σ_T.

5.1 Cover ratio *C/D* and friction angle φ

In the case of $C/D = 0.5$~1.25, Figure 13 shows the variation of σ_T with φ. It can be observed that the σ_T increases gradually with the increase of C/D when the φ is low. However, as the φ increases, the effect of cover ratio on σ_T becomes insignificant. The reason for this phenomenon is due to the following: At small friction angle, the frictional effect along the sliding surface is not apparent, resulting in an increase in σ_T with increasing depth. As the φ gradually increases, the soil arch effect becomes more prominent, leading to a decrease in the effect of C/D on σ_T.

5.2 Cohesion *c*

The influence of the c on the σ_T at different φ is illustrated in Figure 14. It can be seen that the σ_T decreases linearly with the increase of c, and the smaller the φ is, the more sensitive the σ_T is to the change of c. The main reasons for this phenomenon are as follows: Numerical simulations and theoretical studies have shown that the φ plays an important role in the area of collapse zone, and the smaller the φ, the larger the area of the collapse zone and the sliding surface. The energy dissipation of the cohesion occurs mainly at the sliding surface, so the larger the sliding surface area, the more obvious is the reduction of the σ_T as the cohesion increases.

5.3 Surface load P_s

The influence of the P_s on the σ_T for various φ is shown in Figure 15. It is apparent that the σ_T increases linearly as the P_s increases. The increase in the σ_T is small in comparison with the increase in the P_s, and the increase in the σ_T is smaller and smaller with the increase in the φ. At a friction angle of 35°, the surface load will have little effect on the σ_T due to the soil arch effect.

5.4 Friction angle ratio η/φ

The friction angle ratio η/φ is the ratio of the friction angle between the disturbed zone and failure core to the soil friction angle, which is important for the formation of the soil arch. The influence of η/φ on the σ_T is investigated in this section. As shown in Figure 16, for small η/φ the frictional effect of the disturbed zone on the failure core is less and the σ_v is closer to the vertical earth pressure, resulting in a larger σ_T. As η/φ increases, the σ_T gradually decreases. Beyond a certain value, the effect of η/φ on the σ_T is not apparent due to the soil arch effect.

6 Conclusion

Numerical simulation and theoretical Analysis are combined to study the face stability of shallow shield tunnel in sand. Firstly, numerical simulation is used to study the tunnel collapse in sand to obtain the σ_T and shape of collapse zone. The new failure model suitable for shallow tunnel is constructed based on numerical simulations, and the σ_T is solved by upper-bound method. The following conclusions are mainly obtained:

(1) Through numerical simulation, it is found that the σ_T decreases exponentially with the increase of the φ in the range of φ =

25°~40° and C/D = 0.5~1.25. The σ_T increases approximately linearly with the increase of the C/D. And the regression equation is obtained by regression analysis.

(2) Through numerical simulation, it is found that for the sandy soil layer, when the $C/D \le 1$, the can zone can reach ground surface, and the shape of the collapse zone is an inverted round table, which includes a columnar failure core and the rest of the disturbed zone.

(3) A new failure model based on five truncated cones with inverted circular table is proposed. By comparison, it is found that the proposed model is consistent with the numerical model and exiting modes. In addition, the proposed model is more accurate in describing the phenomenon that no soil arch can be formed for shallow tunnel in sand, and it has higher accuracy in solving the σ_T of shallow shield tunnel in sand.

(4) Through the theoretical analysis, it is found that the σ_T decreases nonlinearly with the increase of the φ, and the larger φ is, the more obvious soil arch effect is, and the smaller the effect of C/D on the σ_T is. In addition, the σ_T decreases linearly with the increase of cohesion c, and the smaller φ, the more σ_T sensitive is to the cohesion. The increase of P_S will cause the σ_T to increase, but when the soil arch forms, the effect of P_s on the σ_T is smaller.

Data availability statement

The original contributions presented in the study are included in the article/Supplementary Material, further inquiries can be directed to the corresponding author.

Author contributions

SQ: Project administration, Resources, Writing–original draft. LZ: Conceptualization, Investigation, Writing–original draft. XW: Data curation, Investigation, Writing–original draft. XL: Investigation, Project administration, Writing–original draft. FW: Data curation, Writing–original draft, Writing–review and editing.

Funding

The authors declare financial support was received for the research, authorship, and/or publication of this article. The authors declare financial support was received for the research, authorship, and/or publication of this article. Youth Fund Project of Shanxi Provincial Science and Technology Department, "Research on Flexibility Regulation Mechanism and Engineering Application of NPR Anchor Cables in High Geostress Soft Rock Tunnels.

Conflict of interest

Authors SQ, LZ, XW, and XL were employed by 5TH Engineering LTD. of the First Highway Engineering Bureau CCCC.

Author FW was employed by Shanxi Transportation Technology Research and Development Co., Ltd.

The authors declare that this study received funding from the Science and Technology Project of Shanxi Province Transportation Holding Group Co., Ltd, "Research on Disaster-Causing Mechanism of Coal Mine Subsidence and Prevention and Control of NPR Anchor Cables for Operating Tunnels in Mountainous Areas", Project No.: 2022-JKKJ-6. The funder had the following involvement in the study: decision to publish and preparation of the manuscript.

Publisher's note

References

Anagnostou, G., and Kovári, K. (1994). The face stability of slurry-shield-driven tunnels. *Tunn. Undergr. space Technol.* 9 (2), 165–174. doi:10.1016/0886-7798(94)90028-0

Arthur, L., Darby, A., Rafoneke, B., Daws, G., MacDonald, D., Innaurato, N., et al. (July, 1994). "Face support for a large mix-shield in heterogeneous ground conditions," in Tunnelling'94: Papers presented at the seventh international symposium,'Tunnelling'94' (Springer), London, UK, 531–550.

Atkinson, J., Potts, D., and Schofield, A. (1977). Centrifugal model tests on shallow tunnels in sand. *Tunn. Tunnlng.* 9 (1), 59–64

Chambon, P., and Corte, J.-F. (1994). Shallow tunnels in cohesionless soil: stability of tunnel face. *J. geotechnical Eng.* 120 (7), 1148–1165. doi:10.1061/(asce)0733-9410(1994)120:7(1148)

Chen, R., Tang, L., Ling, D., and Chen, Y. (2011). Face stability analysis of shallow shield tunnels in dry sandy ground using the discrete element method. *Comput. Geotechnics* 38 (2), 187–195. doi:10.1016/j.compgeo.2010.11.003

Chen, R., Yin, X., Tang, L., and Chen, Y. (2018). Centrifugal model tests on face failure of earth pressure balance shield induced by steady state seepage in saturated sandy silt ground. *Tunn. Undergr. Space Technol.* 81, 315–325. doi:10.1016/j.tust.2018.06.031

Chen, R.-P., Li, J., Kong, L.-G., and Tang, L.-J. (2013). Experimental study on face instability of shield tunnel in sand. *Tunn. Undergr. Space Technol.* 33, 12–21. doi:10.1016/j.tust.2012.08.001

Chen, W. F. (1975). *Limit analysis and soil plasticity*. Amsterdam, The Netherlands: Elsevier Science, 1–15.

Di, Q., Li, P., Zhang, M., and Cui, X. (2022a). Influence of relative density on deformation and failure characteristics induced by tunnel face instability in sandy cobble strata. *Eng. Fail. Anal.* 141, 106641. doi:10.1016/j.engfailanal.2022.106641

Di, Q., Li, P., Zhang, M., and Cui, X. (2022b). Investigation of progressive settlement of sandy cobble strata for shield tunnels with different burial depths. *Eng. Fail. Anal.* 141, 106708. doi:10.1016/j.engfailanal.2022.106708

Funatsu, T., Hoshino, T., Sawae, H., and Shimizu, N. (2008). Numerical analysis to better understand the mechanism of the effects of ground supports and reinforcements on the stability of tunnels using the distinct element method. *Tunn. Undergr. Space Technol.* 23 (5), 561–573. doi:10.1016/j.tust.2007.10.003

Han, K., Zhang, C., and Zhang, D. (2016). Upper-bound solutions for the face stability of a shield tunnel in multilayered cohesive–frictional soils. *Comput. Geotechnics* 79, 1–9. doi:10.1016/j.compgeo.2016.05.018

Horn, N. (1961). "Horizontal earth pressure on perpendicular tunnel face," in Proceedings of the Hungarian National Conference of the Foundation Engineer Industry. Budapest

Idinger, G., Aklik, P., Wu, W., and Borja, R. I. (2011). Centrifuge model test on the face stability of shallow tunnel. *Acta Geotech.* 6, 105–117. doi:10.1007/s11440-011-0139-2

Kirsch, A. (2010). Experimental investigation of the face stability of shallow tunnels in sand. *Acta Geotech.* 5, 43–62. doi:10.1007/s11440-010-0110-7

Leca, E., and Dormieux, L. (1990). Upper and lower bound solutions for the face stability of shallow circular tunnels in frictional material. *Géotechnique* 40 (4), 581–606. doi:10.1680/geot.1990.40.4.581

Li, H., Li, X., Fu, J., Zhu, N., Chen, D., Wang, Y., et al. (2023). Experimental study on compressive behavior and failure characteristics of imitation steel fiber concrete under uniaxial load. *Constr. Build. Mater.* 399, 132599. doi:10.1016/j.conbuildmat.2023.132599

Li, H., Tian, X., Song, Z., Wang, J., and Zhou, G. (2018). Study on calculaiton method of digging length for shallow tunnel based on Xie Jiajie's Sourrounding Rock Pressure Formula. *J. Xi'an Univ. Arch. Tech. Nat. Sci. Ed.* 50 (05), 662–667. doi:10.15986/j.1006-7930.2018.05.007

Li, P., Chen, K., Wang, F., and Li, Z. (2019). An upper-bound analytical model of blow-out for a shallow tunnel in sand considering the partial failure within the face. *Tunn. Undergr. Space Technol.* 91, 102989. doi:10.1016/j.tust.2019.05.019

Li, P., Wei, Y., Zhang, M., Huang, Q., and Wang, F. (2022). Influence of non-associated flow rule on passive face instability for shallow shield tunnels. *Tunn. Undergr. Space Technol.* 119, 104202. doi:10.1016/j.tust.2021.104202

Li, P., Zou, H., Wang, F., and Xiong, H. (2020). An analytical mechanism of limit support pressure on cutting face for deep tunnels in the sand. *Comput. Geotechnics* 119, 103372. doi:10.1016/j.compgeo.2019.103372

Liao, S.-M., Liu, J.-H., Wang, R.-L., and Li, Z.-M. (2009). Shield tunneling and environment protection in Shanghai soft ground. *Tunn. Undergr. Space Technol.* 24 (4), 454–465. doi:10.1016/j.tust.2008.12.005

Liu, H., Li, X., Yu, Z., Tan, Y., Ding, Y., Chen, D., et al. (2023a). Influence of hole diameter on mechanical properties and stability of granite rock surrounding tunnels. *Phys. Fluids* 35 (6). doi:10.1063/5.0154872

Liu, S., and Li, X. (2023). Experimental study on the effect of cold soaking with liquid nitrogen on the coal chemical and microstructural characteristics. *Environ. Sci. Pollut. Res.* 30 (13), 36080–36097. doi:10.1007/s11356-022-24821-9

Liu, S., Sun, H., Zhang, D., Yang, K., Li, X., Wang, D., et al. (2023b). Experimental study of effect of liquid nitrogen cold soaking on coal pore structure and fractal characteristics. *Energy* 275, 127470. doi:10.1016/j.energy.2023.127470

Meguid, M., Saada, O., Nunes, M., and Mattar, J. (2008). Physical modeling of tunnels in soft ground: a review. *Tunn. Undergr. Space Technol.* 23 (2), 185–198. doi:10.1016/j.tust.2007.02.003

Messerli, J., Pimentel, E., and Anagnostou, G. (2010). "Experimental study into tunnel face collapse in sand," in *Physical modelling in geotechnics, two volume set* (CRC Press), Boca Raton, FL, USA, 601–606.

Mollon, G., Dias, D., and Soubra, A. H. (2011a). Rotational failure mechanisms for the face stability analysis of tunnels driven by a pressurized shield. *Int. J. Numer. Anal. Methods Geomechanics* 35 (12), 1363–1388. doi:10.1002/nag.962

Mollon, G., Phoon, K. K., Dias, D., and Soubra, A.-H. (2011b). Validation of a new 2D failure mechanism for the stability analysis of a pressurized tunnel face in a spatially varying sand. *J. Eng. Mech.* 137 (1), 8–21. doi:10.1061/(asce)em.1943-7889.0000196

Murayama, S., Endo, M., Hashiba, T., Yamamoto, K., and Sasaki, H. (August, 1996). "Geotechnical aspects for the excavating performance of the shield machines," in The 21st annual lecture in meeting of Japan Society of Civil Engineers). Japan.

Senent, S., Mollon, G., and Jimenez, R. (2013). Tunnel face stability in heavily fractured rock masses that follow the Hoek–Brown failure criterion. *Int. J. Rock Mech. Min. Sci.* 60, 440–451. doi:10.1016/j.ijrmms.2013.01.004

Soubra, A.-H., Dias, D., Emeriault, F., and Kastner, R. (March, 2008). "Three-dimensional face stability analysis of circular tunnels by a kinematical approach," in GeoCongress 2008: characterization, monitoring, and modeling of GeoSystems, New Orleans, LA, USA, 894–901.

Wang, F. N., Guo, Z., Qiao, X., Fan, J., Li, W., Mi, M., et al. (2021a). Large deformation mechanism of thin-layered carbonaceous slate and energy coupling support technology of NPR anchor cable in Minxian Tunnel: a case study. *Tunn. Undergr. Space Technol.* 117, 104151. doi:10.1016/j.tust.2021.104151

Wang, F. N., Yin, S., Guo, A., Wang, Z., Mi, M., Qi, G., et al. (2021b). Frame structure and engineering applications of the multisource system cloud service platform of monitoring of the soft rock tunnel. *Geofluids* 2021, 1–15. doi:10.1155/2021/6672732

Yu, L., Zhang, D., Fang, Q., Cao, L., Zhang, Y., and Xu, T. (2020). Face stability of shallow tunnelling in sandy soil considering unsupported length. *Tunn. Undergr. Space Technol.* 102, 103445. doi:10.1016/j.tust.2020.103445

Zhang, J., Li, X., Qin, Q., Wang, Y., and Gao, X. (2023). Study on overlying strata movement patterns and mechanisms in super-large mining height stopes. *Bull. Eng. Geol. Environ.* 82 (4), 142. doi:10.1007/s10064-023-03185-5

Zhang, X., Wang, M., Wang, Z., Li, J., Tong, J., and Liu, D. (2020). A limit equilibrium model for the reinforced face stability analysis of a shallow tunnel in cohesive-frictional soils. *Tunn. Undergr. Space Technol.* 105, 103562. doi:10.1016/j.tust.2020.103562

Zhang, C., Han, K., and Zhang, D. (2015). Face stability analysis of shallow circular tunnels in cohesive-frictional soils. *Tunn. Undergr. Space Technol.* 50, 345–357.

Zhang, Z., Hu, X., and Scott, K. D. (2011). A discrete numerical approach for modeling face stability in slurry shield tunnelling in soft soils. *Comput. Geotechnics* 38 (1), 94–104. doi:10.1016/j.compgeo.2010.10.011